INTERNATIONAL JOURNAL FOR NUMERICAL METHODS IN FLUIDS
Int. J. Numer. Meth. Fluids 2001; **35**: 643–667

Computation of two-dimensional flows past ram-air parachutes

S. Mittal*,[1], P. Saxena and A. Singh

Department of Aerospace Engineering, Indian Institute of Technology, Kanpur, India

SUMMARY

Computational results for flow past a two-dimensional model of a ram-air parachute with leading edge cut are presented. Both laminar ($Re = 10^4$) and turbulent ($Re = 10^6$) flows are computed. A well-proven stabilized finite element method (FEM), which has been applied to various flow problems earlier, is utilized to solve the incompressible Navier–Stokes equations in the primitive variables formulation. The Baldwin–Lomax model is employed for turbulence closure. Turbulent flow computations past a Clarck-Y airfoil without a leading edge cut, for $\alpha = 7.5°$, result in an attached flow. The leading edge cut causes the flow to become unsteady and leads to a significant loss in lift and an increase in drag. The flow inside the parafoil cell remains almost stagnant, resulting in a high value of pressure, which is responsible for giving the parafoil its shape. The value of the lift-to-drag ratio obtained with the present computations is in good agreement with those reported in the literature. The effect of the size and location of the leading edge cut is studied. It is found that the flow on the upper surface of the parafoil is fairly insensitive to the configuration of the cut. However, the flow quality on the lower surface improves as the leading edge cut becomes smaller. The lift-to-drag ratio for various configurations of the leading edge cut varies between 3.4 and 5.8. It is observed that even though the time histories of the aerodynamic coefficients from the laminar and turbulent flow computations are quite different, their time-averaged values are quite similar. Copyright © 2001 John Wiley & Sons, Ltd.

KEY WORDS: leading edge cut; lift-to-drag ratio; ram-air parachute; unsteady turbulent flows

1. INTRODUCTION

Parachutes are used in a wide variety of applications, including sports activities, payload recovery, military applications and flood relief efforts. Ram-air parachutes have been quite popular with the sports community. Unlike the conventional round canopy parachutes, they have a large lift-to-drag ratio and, therefore, possess a high degree of maneuverability. Recently, defense organizations all over the world have shown a lot of interest in deploying

* Correspondence to: Department of Aerospace Engineering, Indian Institute of Technology, Kanpur, UP 208016, India.
[1] E-mail: smittal@iitk.ac.in

Received 12 July 1999
Revised 3 April 2000

these types of parachutes for various applications. An overview of the technological issues involved in parachutes can be found in the article by Dennis [1]. Applications of the parafoil (ram-air parachutes) have been described in the review article by Nicolaides *et al.* [2].

The aerodynamics of parachutes is very complex. It involves three-dimensional unsteady turbulent flows past rapidly deforming boundaries. The ram-air parachute is a flying wing made out of a very low porosity fabric and composed of various cells, which give the wing its shape. Pennants along the lower surface of the parafoil transfer the aerodynamic load to the suspension lines and also aid in improving the lateral stability of the vehicle. They are also useful in improving the aerodynamic efficiency of the parafoil by preventing/minimizing the spanwise flow of air. It is desirable for a parafoil to have the lift-to-drag ratio (L/D) as large as possible for good aerodynamic performance. The L/D ratio is related to the glide angle of the parachute. A parachute with a large L/D will, typically, have good range and endurance qualities. More on the aerodynamics of parafoils can be found in the article by Lingard [3].

The aerodynamic design of parachutes is largely an empirical process and the database has mostly been generated via wind tunnel and drop tests. Recently, there have been some advances towards the numerical prediction of parachute aerodynamics. The review article by Strickland and Higuchi [4] is a good description of the present state-of-the-art capabilities for predicting aerodynamic performance of parachutes. Benney and Stein [5] have developed a computational model for the fluid–structure interaction during the inflation stage of the 'round' canopy parachutes. Their computations assume axisymmetric deformation of the canopy during inflation. Garrard *et al.* [6] and Tezduyar *et al.* [7] have used finite element methods (FEMs) to study the aerodynamics of the ram-air parachutes for the steady state glide phase and during the inflation stage. Tezduyar *et al.* [8] have reported their computations for a parafoil with prescribed shape changes. As an example they have presented results for the simulation of a flare maneuver in which the flaps are deployed to reduce the speed of the parafoil. These computations have been carried out in three dimensions and incorporate some of the details of the parafoil geometry, such as the number of cells, aspect ratio and curvature. The parafoil section, however, is assumed to be a complete airfoil without a leading edge cut. Ross [9] has utilized potential flow computations in two and three dimensions to study the effect of the leading edge cut for the *LS*1-0417 airfoil. His results indicate an improved performance with a reduction in the size of the leading edge cut. The two-dimensional Navier–Stokes computations indicate a further improvement in performance if the trailing edge of the *LS*-0417 airfoil is rounded.

The typical trajectory of a parafoil consists of the inflation stage, steady state glide phase and the flare maneuver for touchdown. Most of the flight time is spent in the steady state glide stage. The aerodynamic performance of the parafoil in this stage is extremely important for the success of the overall design of the parafoil. A basic airfoil section that has a good lift-to-drag ratio is chosen and a cut is applied at its leading edge. The leading edge cut allows the air to ram in and causes the fabric to take its desired aerodynamic shape. The location and size of the cut play important roles in the performance of the parachute system. A small-sized cut placed close to the stagnation point of the basic airfoil section will cause little change to the airflow and is desirable from the point of view of good aerodynamic performance. However, too small a leading edge cut may lead to a longer (and sometimes unacceptable) duration of inflation time of the parachute. A very large cut leads to poor aerodynamic performance and

is associated with large snatch force on the parachute during inflation due to the shorter inflation time. This is undesirable from the point of view of the design of suspension lines. An optimal size of the leading edge cut is one of the key ingredients of the ram-air parachute design.

In the present study, the effect of the leading edge cut on the aerodynamic performance of the parachute is investigated. Stabilized finite element formulation for the two-dimensional incompressible Navier–Stokes equations is utilized to compute flow past a ram-air parachute with a Clarck-Y section. This airfoil section is quite popular with the parafoil designers because of its relative ease in fabrication. Other airfoil sections, which give better aerodynamic performance have also been used by designers. The methodologies followed in this article can be applied to a parafoil with any arbitrary airfoil section. The finite element mesh consists of a structured mesh close to the body and an unstructured part, generated via Delaunay's triangulation, away from the body. This type of a grid has the ability of handling fairly complex geometries while still providing the desired resolution close to the body to effectively capture the boundary layer flow. In the present study this type of grid enables the investigation of the effect of the various configurations of the leading edge cut. Computations are carried out for both laminar and turbulent flows. Turbulent flows are modeled using an algebraic model for closure. The Baldwin–Lomax turbulence model [10] has been implemented and has been validated on an NACA 0012 airfoil quite extensively. The implementation of the Baldwin–Lomax model in the context of unstructured grids is not trivial. The interested reader is referred to the articles by Kallinderis [11], Mavriplis [12] and Anderson and Bonhaus [13] for details. Our results for the NACA 0012 airfoil (not reported here) are in good agreement with those from other researchers. Preliminary computations indicate the ability of our formulations and their implementations to capture the phenomenon of *hysteresis*, which occurs close to the stall angle of the airfoil [14]. These will be reported in a separate article.

Laminar flow calculations ($Re = 10^4$) for a ram-air section with a cut at 10 per cent chord length from the leading edge and at a 45° angle with the free-stream direction have been carried out for various angles of attack. In all cases, separated unsteady flow is observed. The fabric of the parafoil is assumed to be impervious and of negligible thickness. However, the nodes lying on the parafoil surface are duplicated to allow for the different values of pressure on the interior and exterior of the fabric. Turbulent flow computations ($Re = 10^6$) for a clean Clarck-Y section (without a leading edge cut) result in a flow that is attached on the major part of the airfoil. The pressure distribution compares well with that from the inviscid flow theory obtained from a panel code. The Clarck-Y section with a leading edge cut results in unsteady flow, even for $\alpha = 0°$. The effect of the cut geometry and location is investigated. It is found that the location of the cut that is closer to the leading edge of the parafoil results in better values of the lift to drag ratio.

The outline of the rest of the article is as follows. Section 2 reviews the governing equations for incompressible fluid flow. The streamline-upwind/Petrov–Galerkin (SUPG) and pressure-stabilizing/Petrov–Galerkin (PSPG) stabilization techniques [15–17] are employed to stabilize computations against spurious numerical oscillations and to enable the use of equal-order interpolation velocity–pressure elements. Section 3 describes the finite element formulation incorporating these stabilizing terms. In Section 4, computational results for the flows involving ram-air parachutes are presented and discussed. Section 5 contains some concluding remarks.

2. THE GOVERNING EQUATIONS

Let $\Omega \subset \mathbb{R}^{n_{sd}}$ and $(0, T)$ be the spatial and temporal domains respectively, where n_{sd} is the number of space dimensions, and let Γ denote the boundary of Ω. The spatial and temporal co-ordinates are denoted by $\mathbf{x}$ and t. The Navier–Stokes equations governing incompressible fluid flow are

$$\rho\left(\frac{\partial \mathbf{u}}{\partial t} + \mathbf{u}\cdot\nabla\mathbf{u} - \mathbf{f}\right) - \nabla\cdot\boldsymbol{\sigma} = 0 \quad \text{on } \Omega \text{ for } (0, T) \tag{1}$$

$$\nabla\cdot\mathbf{u} = 0 \quad \text{on } \Omega \text{ for } (0, T) \tag{2}$$

Here ρ, $\mathbf{u}$, $\mathbf{f}$ and $\boldsymbol{\sigma}$ are the density, velocity, body force and the stress tensor respectively. The stress tensor is written as the sum of its isotropic and deviatoric parts

$$\boldsymbol{\sigma} = -p\mathbf{I} + \mathbf{T}; \quad \mathbf{T} = 2\mu\boldsymbol{\varepsilon}(\mathbf{u}), \quad \boldsymbol{\varepsilon}(\mathbf{u}) = \frac{1}{2}((\nabla\mathbf{u}) + (\nabla\mathbf{u})^T) \tag{3}$$

where p and μ are the pressure and viscosity respectively. Both the Dirichlet and Neumann-type boundary conditions are accounted for, represented as

$$\mathbf{u} = \mathbf{g} \quad \text{on } \Gamma_g, \qquad \mathsf{n}\cdot\boldsymbol{\sigma} = \mathbf{h} \quad \text{on } \Gamma_h \tag{4}$$

where Γ_g and Γ_h are complementary subsets of the boundary Γ. The initial condition on the velocity is specified on Ω

$$\mathbf{u}(\mathbf{x}, 0) = \mathbf{u}_0 \quad \text{on } \Omega \tag{5}$$

where $\mathbf{u}_0$ is divergence free.

3. FINITE ELEMENT FORMULATION

Consider a finite element discretization of Ω into subdomains Ω^e, $e = 1, 2, \ldots, n_{el}$, where n_{el} is the number of elements. Based on this discretization, for velocity and pressure we define the finite element trail function spaces $\mathscr{S}_{\mathbf{u}}^h$ and $\mathscr{S}_p^h$, and weighting function spaces $\mathscr{V}_{\mathbf{u}}^h$ and $\mathscr{V}_p^h$. These function spaces are selected by taking the Dirichlet boundary conditions into account as subsets of $[\mathbf{H}^{1h}(\Omega)]^{n_{sd}}$ and $\mathbf{H}^{1h}(\Omega)$, where $\mathbf{H}^{1h}(\Omega)$ is the finite-dimensional function space over Ω. The stabilized finite element formulation of Equations (1) and (2) is written as follows: find $\mathbf{u}^h \in \mathscr{S}_{\mathbf{u}}^h$ and $p^h \in \mathscr{S}_p^h$ such that $\forall \mathbf{w}^h \in \mathscr{V}_{\mathbf{u}}^h$, $q^h \in \mathscr{V}_p^h$

$$\int_\Omega \mathbf{w}^h\cdot\rho\left(\frac{\partial \mathbf{u}^h}{\partial t} + \mathbf{u}^h\cdot\nabla\mathbf{u}^h - \mathbf{f}\right) d\Omega + \int_\Omega \boldsymbol{\varepsilon}(\mathbf{w}^h):\ \boldsymbol{\sigma}(p^h, \mathbf{u}^h)\, d\Omega$$

$$+\int_{\Omega} q^h \nabla\cdot\mathbf{u}^h \,\mathrm{d}\Omega + \sum_{e=1}^{n_{\mathrm{el}}} \int_{\Omega^e} \frac{1}{\rho}\left(\tau_{\mathrm{SUPG}}\rho\,\mathbf{u}^h\cdot\nabla\mathbf{w}^h + \tau_{\mathrm{PSPG}}\nabla q^h\right)$$

$$\cdot\left[\rho\left(\frac{\partial\mathbf{u}^h}{\partial t} + \mathbf{u}^h\cdot\nabla\mathbf{u}^h - \mathbf{f}\right) - \nabla\cdot\boldsymbol{\sigma}(p^h, \mathbf{u}^h)\right]\mathrm{d}\Omega^e$$

$$+\sum_{e=1}^{n_{\mathrm{el}}} \int_{\Omega^e} \delta\nabla\cdot\mathbf{w}^h\rho\nabla\cdot\mathbf{u}^h \,\mathrm{d}\Omega^e = \int_{\Gamma_h} \mathbf{w}^h\cdot\mathbf{h}^h \,\mathrm{d}\Gamma \tag{6}$$

In the variational formulation given by Equation (6), the first three terms and the right-hand side constitute the Galerkin formulation of the problem. The first series of element-level integrals are the SUPG and PSPG stabilization terms added to the variational formulations [15]. In the current formulation, τ_{PSPG} is the same as τ_{PSPG} and is given as

$$\tau = \left(\left(\frac{2\|\mathbf{u}^h\|}{h}\right)^2 + \left(\frac{4\nu}{h^2}\right)^2\right)^{-1/2} \tag{7}$$

The second series of element-level integrals are added to the formulation for numerical stability at high Reynolds numbers. This is a least-squares term based on the continuity equation. The coefficient δ is defined as

$$\delta = \frac{h}{2}\|\mathbf{u}^h\| z \tag{8}$$

$$z = \begin{cases} \left(\dfrac{Re_u}{3}\right) & Re_u \le 3 \\ 1 & Re_u > 3 \end{cases} \tag{9}$$

and Re_u is the cell Reynolds number. Both stabilization terms are weighted residuals and therefore maintain the consistency of the formulation. h is the *element length* and various definitions have been used by researchers in the past. Mittal [18] conducted a systematic numerical study to investigate the effect of high aspect ratio elements on the performance of the finite element formulation for three commonly used definitions of h. The one which results in the lowest sensitivity of the computed flow to the element aspect ratio has been used for computations in the present work. According to this definition, the element length is equal to the minimum edge length of a triangular (three-noded) element.

4. RESULTS AND DISCUSSIONS

All the computations reported in this article are carried out on the *Digital* and *Silicon Graphics* workstations at IIT Kanpur in 64-bit precision. Equal-in-order linear basis functions for velocity and pressure (the *P1P1* element) are used and a three-point quadrature is employed

for numerical integration. The non-linear equation systems resulting from the finite element discretization of the flow equations are solved using the Generalized Minimal RESidual (GMRES) technique [19] in conjunction with diagonal preconditioners. The formulations and their implementations used in the present work are well proven and have been utilized to solve a variety of flow problems [15,18,20–23]. For example, they have been used to solve $Re = 100$ flow past an isolated circular cylinder. This has become a standard benchmark problem, and various researchers in the past have reported their computed results that were in good agreement with experimental observations. All turbulent flow computations reported in this article have utilized the Baldwin–Lomax model for turbulence closure.

The two-dimensional model of the ram-air parafoil resides in a rectangular computational domain, whose upstream and downstream boundaries are located at 5 and 11 chord lengths from the leading edge respectively. The upper and lower boundaries are placed at 5 chord lengths each from the leading edge. The no-slip condition is specified for the velocity on the parafoil surface while free-stream values are assigned for the velocity at the upstream boundary. At the downstream boundary, a Neumann-type boundary condition is specified for the velocity, which corresponds to zero viscous stress vector. On the upper and lower surface boundaries the component of velocity normal to the component of stress vector along these boundaries is prescribed a zero value. The basic section for the ram-air parafoil is the 12 per cent thick *Clarck-Y* section. Figure 1 shows the schematic of the flow past a two-dimensional section of a ram-air parachute placed at an angle of attack (α) to the free-stream flow. The location and size of the leading edge cut are denoted by x_{cut} and θ_{cut} respectively. x_{cut} is the distance measured from the leading edge of the airfoil along the chord length where the cut is applied and θ_{cut} is the angle of the cut with the free-stream direction. The Reynolds number is based on the chord length of the airfoil, free-stream velocity and viscosity of the fluid.

First, results are presented for $Re = 10^6$ turbulent flow past a clean *Clarck-Y* airfoil at 7.5° angle of attack. The results from the computation are compared with those from a panel method for inviscid flow using linear vortex distribution [24]. Next, laminar flow computations ($Re = 10^4$) for a ram-air parachute with $x_{\text{cut}} = 0.1c$ and $\theta_{\text{cut}} = 135°$ are carried out at various angles of attack. Results for turbulent flow computations ($Re = 10^6$) for various angles of attack are presented next. Finally, results are presented for the effect of the location and size of the leading edge cut. All the values for the lift and drag coefficients and the Strouhal number reported in this article have been non-dimensionalized with respect to the chord length of the clean airfoil (without the cut) and free-stream speed.

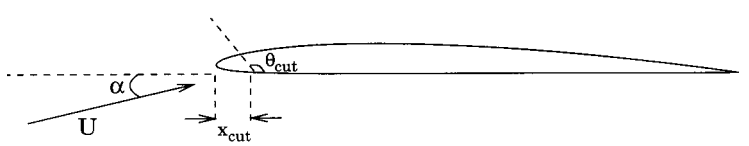

Figure 1. Flow past a ram-air parafoil: schematic.

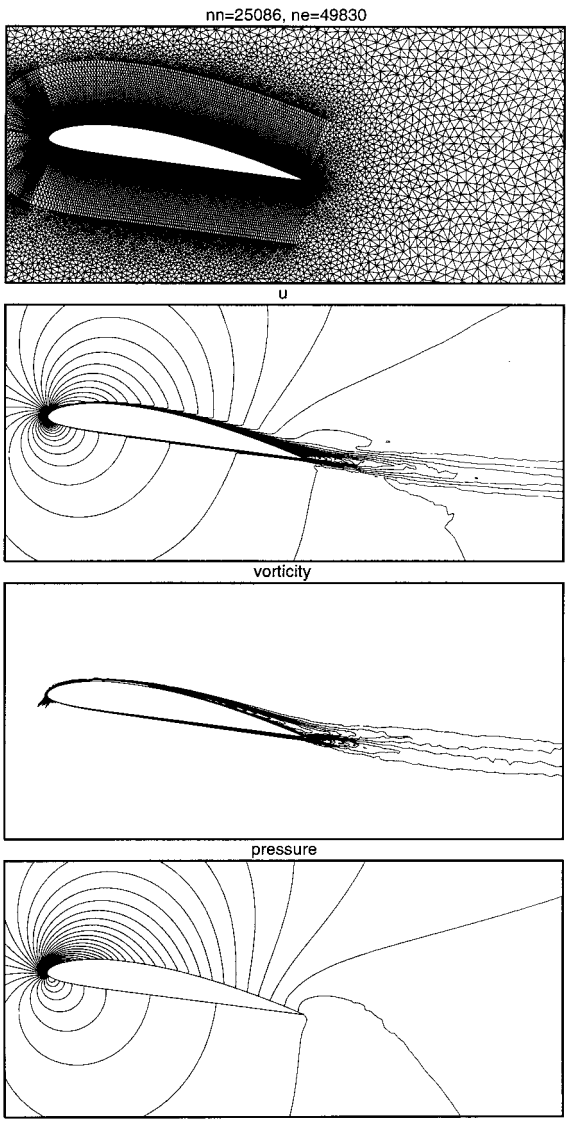

Figure 2. $Re = 10^6$, $\alpha = 7.5°$ turbulent flow past a Clarck-Y airfoil: close-up view of the finite element mesh and the x component of velocity, vorticity and pressure fields for the steady state solution (nn, number of nodes; ne, number of elements).

4.1. Flow past a Clarck-Y airfoil

Figure 2 shows the finite element mesh and the x component of velocity, vorticity and pressure fields for the steady state solution past a clean Clarck-Y airfoil at 7.5° angle of attack. The Reynolds number is 10^6 and the flow has been computed with the Baldwin–Lomax turbulence model. To resolve adequately the high gradients in the flow close to the airfoil, a structured finite element mesh is generated near the body. An unstructured mesh is generated using Delaunay's technique in the rest of the domain via an automatic mesh generator to reduce the number of grid points and to avoid the difficulties in generating a structured mesh around arbitrary geometries. The finite element mesh used in the present case consists of 25086 nodes and 49830 triangular elements. From the figure it can be observed that the flow is attached to the airfoil except for a small region near the trailing edge on the upper surface. The steady state lift and drag coefficients are 1.38 and 0.0204 respectively. A panel method with linear vortex distribution [24] is employed to compare the inviscid flow solution with the viscous solution obtained with the Reynolds-averaged Navier–Stokes (RANS) equations. It is well known that for non-separated flows the pressure distribution from the inviscid flow solution is quite close to that from the viscous flow at high Reynolds numbers. Figure 3 shows the variation of the lift coefficient for the Clarck-Y airfoil for various angles of attack. For $\alpha = 7.5°$, the inviscid solution overpredict the lift coefficient by approximately 13 per cent. Figure 4 shows the variation of the pressure coefficient along the airfoil surface for the steady state solutions obtained with the linear vortex panel method and the RANS for $\alpha = 7.5°$. As expected, for non-separated flows the two methods result in very similar pressure distributions. The presence of boundary layer results in a lower suction peak on the upper surface of the airfoil, which is responsible for the loss in lift compared with the inviscid flow case. The

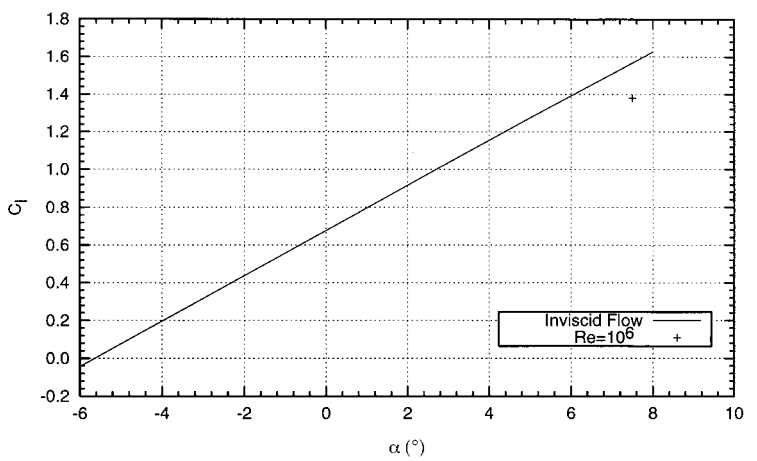

Figure 3. Inviscid flow past a Clarck-Y airfoil computed using panel method with linear vortex distribution: variation of the lift coefficient with the angle of attack. Also shown is the solution obtained with the RANS ($Re = 10^6$).

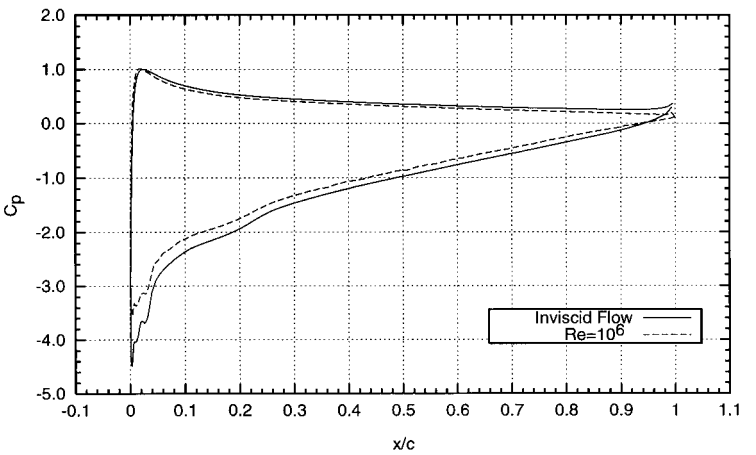

Figure 4. Flow past a Clarck-Y airfoil at $\alpha = 7.5°$: variation of the pressure coefficient along the airfoil surface for the steady state solutions obtained with the linear vortex panel method and the RANS ($Re = 10^6$).

computations for the inviscid flows have been carried out with 150 panels. Computations with twice the number of panels result in almost indistinguishable solutions. These computations, in addition to providing the comparison between viscous and inviscid solutions, increase confidence in the finite element formulation and its implementation for viscous flows.

4.2. $x_{cut} = 0.1c$, $\theta = 135°$, $Re = 10^4$ laminar flow past a ram-air parafoil

Results are presented for laminar flow past a ram-air parafoil at various angles of attack with the turbulence model switched off. The section of the ram-air parafoil is obtained from the Clarck-Y airfoil with $x_{\text{cut}} = 0.1c$ and $\theta_{\text{cut}} = 135°$. The sharp corners at the leading edge cut of the parafoil are expected to result in separated flows. The motivation to carry out laminar flow computations is to see if the time-averaged values of the aerodynamic coefficients show any resemblance to those obtained with a turbulence closure. Figure 5 shows a typical finite element mesh and its close-ups employed for the computations in this article. To study the effect of the cut, flow inside and outside the parafoil is simulated. As is the case with the Clarck-Y airfoil, a structured mesh is employed close to the body and the rest of the domain is filled with triangles via an automatic mesh generator using Delaunay's algorithm. It is assumed that the fabric that forms the parafoil is impervious and no-slip conditions are applied to the velocity on the parafoil surface. The thickness of the fabric is neglected. However, to simulate the pressure differential across the fabric, two sets of nodes, one for the outer and the other for the internal flow, are utilized. To study the effect of the discretization near the leading edge cut, computations have been carried out with a finer mesh in that region. No appreciable effect of the mesh is observed.

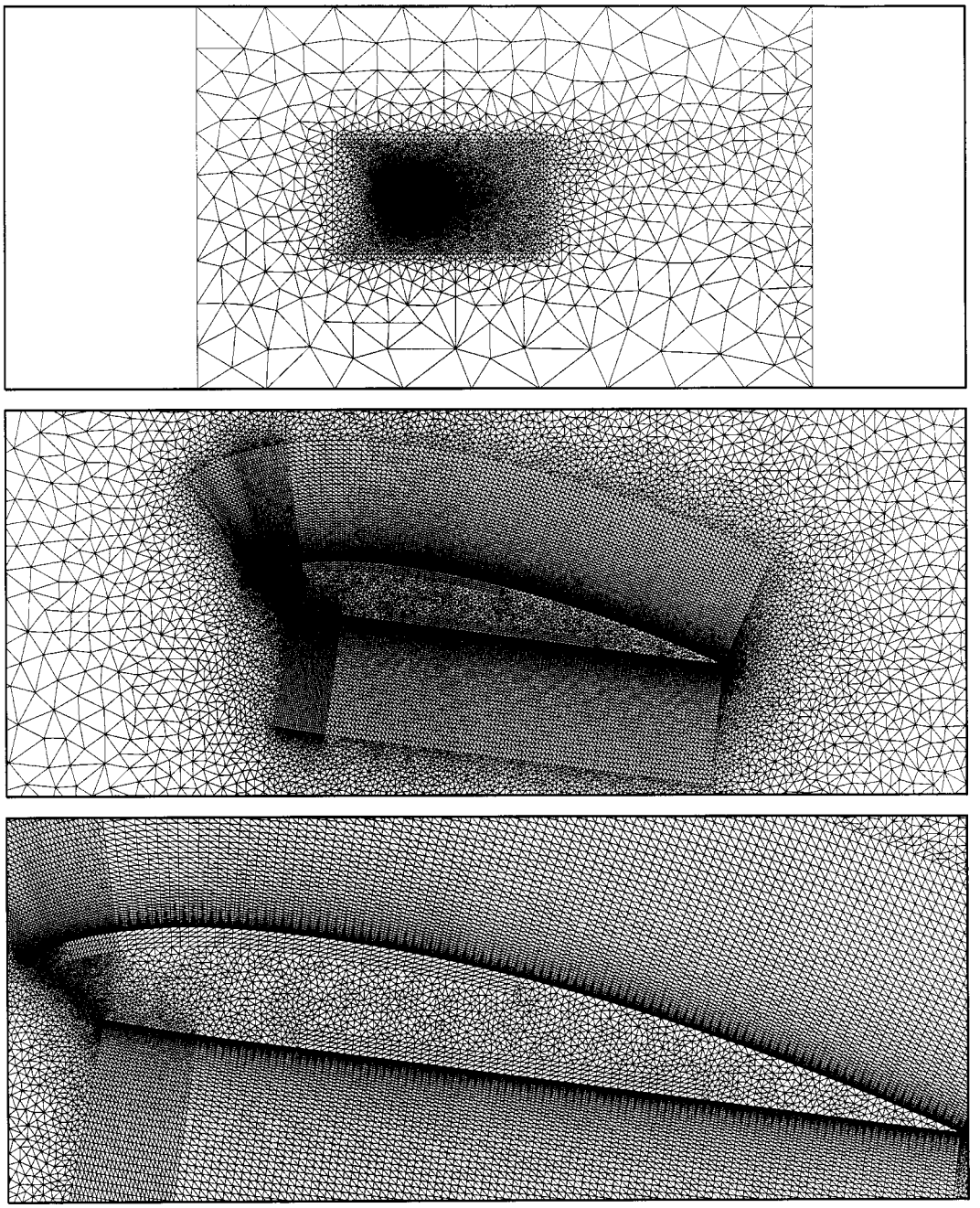

Figure 5. Flow past a ram-air parafoil: a typical finite element mesh employed for the computations and its close-up views. The mesh consists of 26789 nodes and 53020 triangular elements.

Plate 1 shows the vorticity and pressure fields corresponding to the peak value of the lift coefficient for the developed unsteady solution at various angles of attack. The various angles of attack considered are $\alpha = 2°$, 5°, 7°, 10° and 15°. It can be observed that the vortex-shedding pattern changes significantly with the angle of attack. As the angle of attack increases, the vortex-shedding frequency decreases and vortices become stronger. The interaction of the strong vortices with each other and the surface of the body leads to complex flow patterns and a departure of the flow field from temporal periodicity. At low angles of attack, the flow separates both on the lower and upper surfaces of the parafoil. For example, for $\alpha = 2°$ the flow on the upper surface flow separates near the quarter chord point. The shear layer rolls up and leads to vortex formation and its shedding near the trailing edge. On the lower surface the vortices are formed close to the leading edge and travel downstream. However, at larger angles of attack, the flow on the lower surface stays attached but it separates on the upper surface right at the leading edge of the cut. In the images shown in Plate 1, the red color corresponds to large values of pressure and counter-clockwise rotating vortices, while the blue color denotes low pressure and clockwise rotating vortices. It can be observed that the fluid inside the parafoil is virtually stagnant and therefore the high pressure that is responsible for inflating the parafoil and giving its shape is achieved. At large angles of attack the flow separation at the leading edge results in the formation of unsteady vortical structures that are associated with low pressure cores. These dynamic low-pressure zones contribute to the unsteady lift acting on the parafoil. Figure 6 shows the time histories of the lift and drag coefficients for the computations at various angles of attack. The time-averaged value of the aerodynamic coefficients is also shown in the figure. As expected, the average value of the drag coefficient increases with the angle of attack. The lift coefficient, however, increases untill a certain point and then decreases. The unsteady component of the aerodynamic coefficients also increases with the angle of attack signifying an increased vortical activity. Compared with $\alpha = 10°$, the average lift coefficient for $\alpha = 15°$ is lower and the drag coefficient significantly higher. This suggests the correspondence of the $\alpha = 15°$ case with the post-stall regime of the flow. To highlight the effect of angle of attack, flow pictures during one cycle of the lift coefficient variation are shown in Figures 7 and 8 for $\alpha = 5°$ and 15° respectively. The wake for $\alpha = 5°$ is much narrower and more organized compared with that for $\alpha = 15°$. Massively separated flow on the upper surface, right at the leading edge of the parafoil, is observed for $\alpha = 15°$. In both the cases, the flow on the lower surface of the parafoil separates at the leading edge and then reattaches further downstream. During each cycle of the time variation of the lift coefficient, one counter-clockwise rotating vortex is released from the lower surface at the trailing edge. For the $\alpha = 5°$ flow, the shear layer that is formed due to the separation of the flow at the leading edge of the upper surface of the parafoil rolls up, due to the Kelvin–Helmoltz instability, and a clockwise rotating vortex is released during each cycle of the variation of the lift coefficient. The interaction between the vortex that is released, the one that is forming and the airfoil surface leads to an interesting dynamics and is responsible for the upward deflection of the entire wake with respect to the free-stream flow direction. Such type of a behavior has also been reported earlier by Mittal and Tezduyar [25] for $Re = 5000$, $\alpha = 10°$ flow past a NACA 0012 airfoil, and by Behr [26] for flow past a circular cylinder at similar Reynolds numbers. The flow on the upper surface of the parafoil for the $\alpha = 15°$ case is even more complex and a series of secondary and tertiary vortices are induced as a result of the vortex–vortex and vortex–surface interactions.

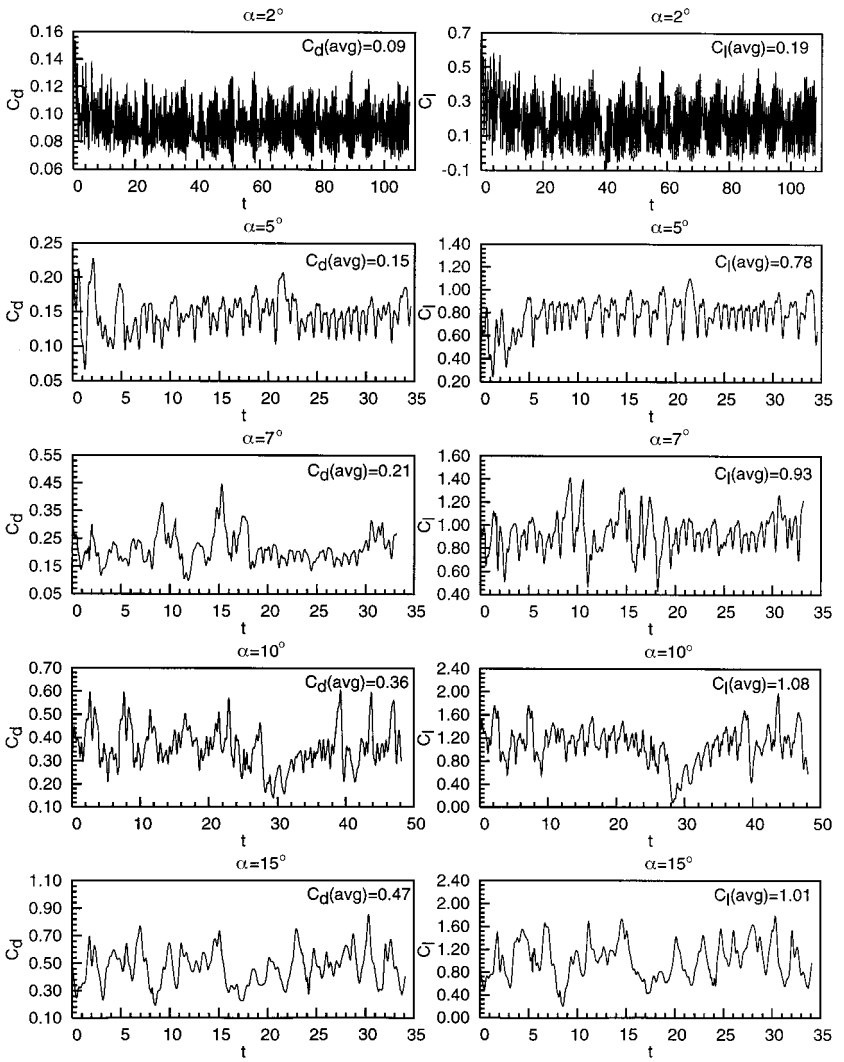

Figure 6. $Re = 10^4$ laminar flow past a ram-air parafoil with $x_{\text{cut}} = 0.1c$ and $\theta_{\text{cut}} = 135°$ at various angles of attack: time histories of the lift and drag coefficients.

4.3. $x_{cut} = 0.1c$, $\theta_{cut} = 135°$, $Re = 10^6$ turbulent flow past a ram-air parafoil

Turbulent flow past a parafoil with the same leading edge cut as in the previous section is computed for $\alpha = 0°$, 7.5° and 10°. Figure 9 shows the vorticity and pressure fields during one cycle of the lift coefficient for the temporally periodic solution for $\alpha = 0°$. Qualitatively, the flow pattern for this case is quite similar to that in Plate 1 for laminar flow at $\alpha = 2°$. On the

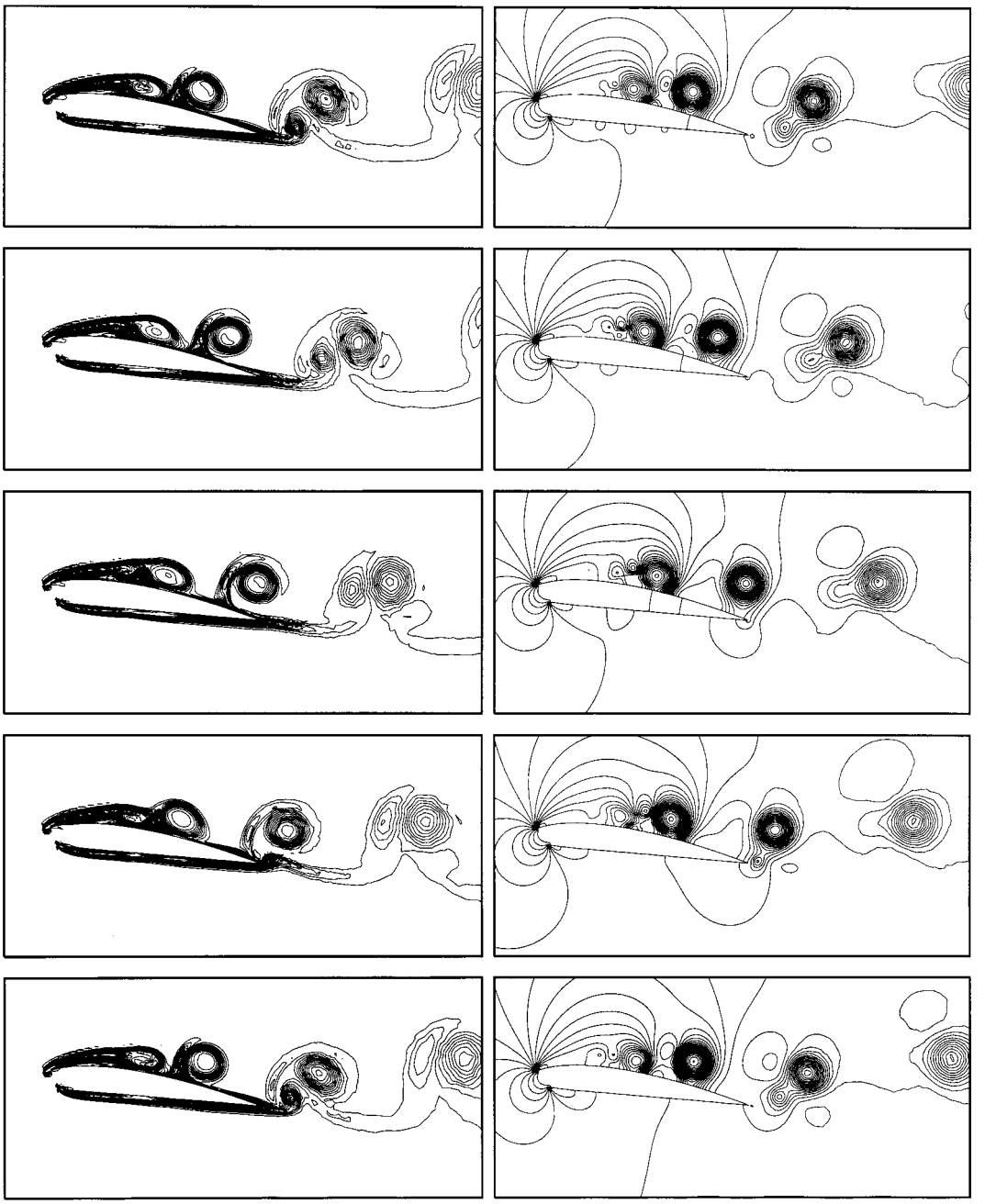

Figure 7. $Re = 10^4$ laminar flow past a ram-air parafoil with $x_{cut} = 0.1c$ and $\theta_{cut} = 135°$ at $\alpha = 5°$: vorticity (left) and pressure (right) fields during one cycle of the lift coefficient variation for the developed unsteady solution.

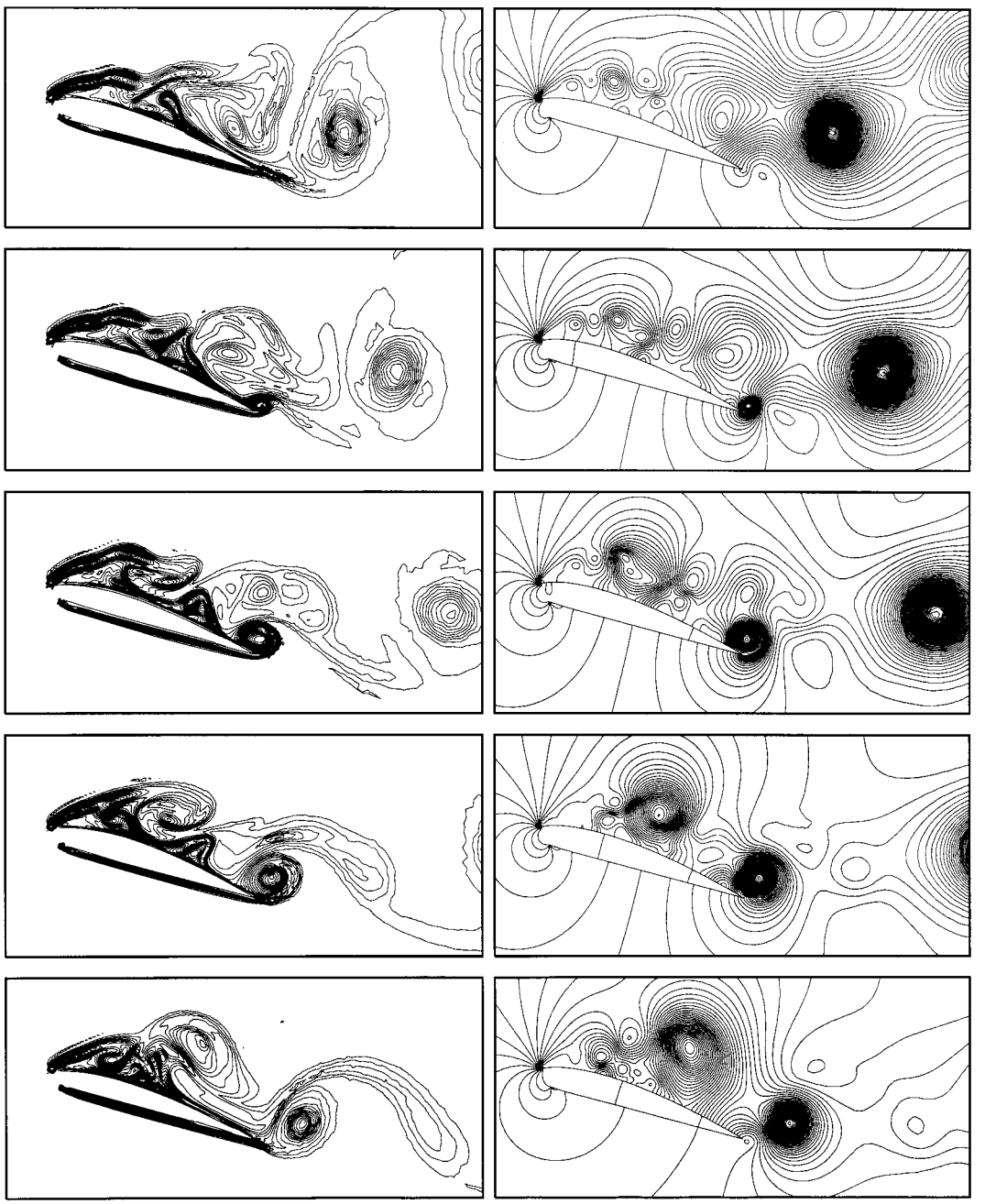

Figure 8. $Re = 10^4$ laminar flow past a ram-air parafoil with $x_{cut} = 0.1c$ and $\theta_{cut} = 135°$ at $\alpha = 15°$: vorticity (left) and pressure (right) fields during one cycle of the lift coefficient variation for the developed unsteady solution.

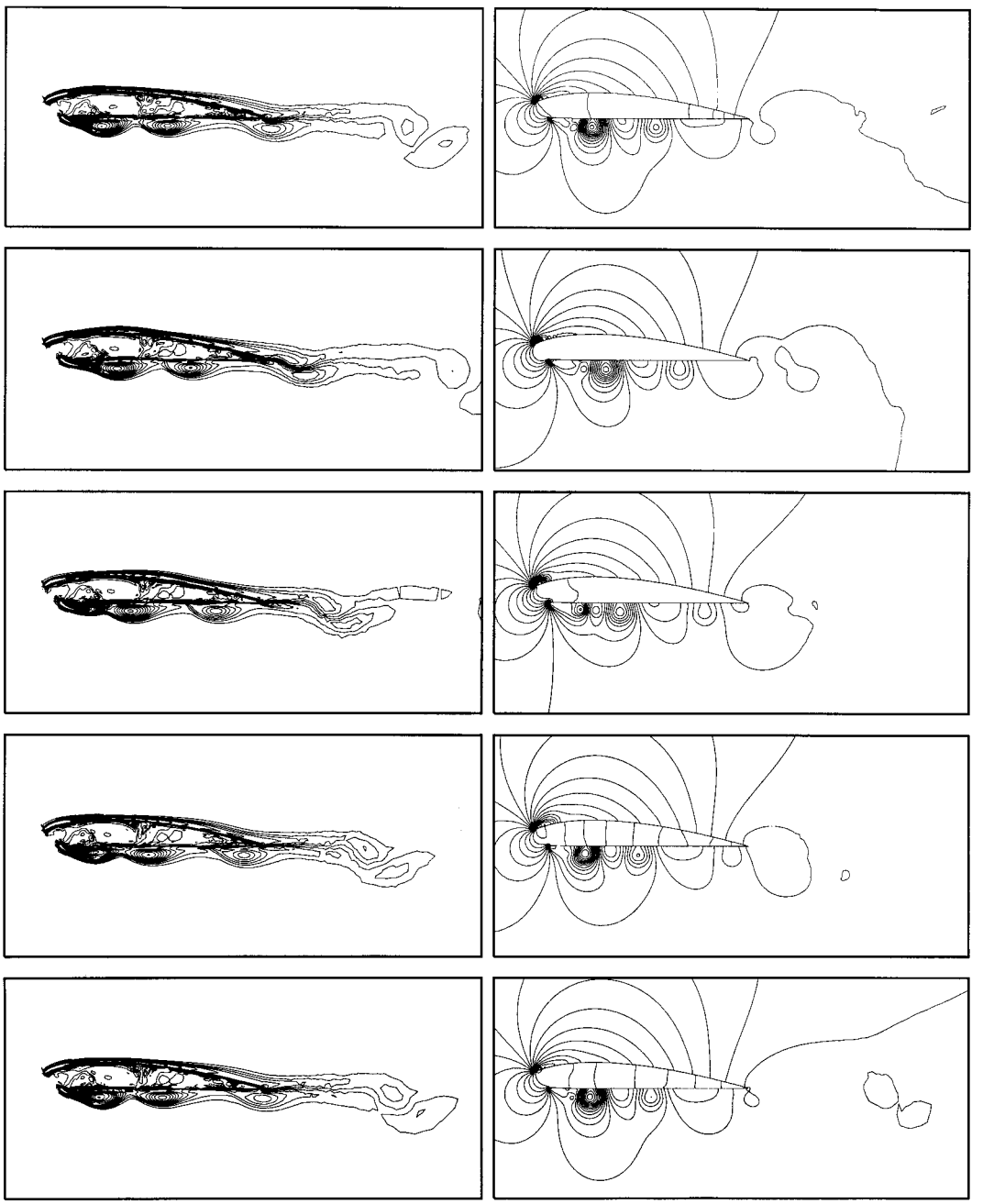

Figure 9. $Re = 10^6$ turbulent flow past a ram-air parafoil with $x_{\text{cut}} = 0.1c$ and $\theta_{\text{cut}} = 135°$ at $\alpha = 0°$: vorticity (left) and pressure (right) fields during one cycle of the lift coefficient variation for the temporally periodic solution.

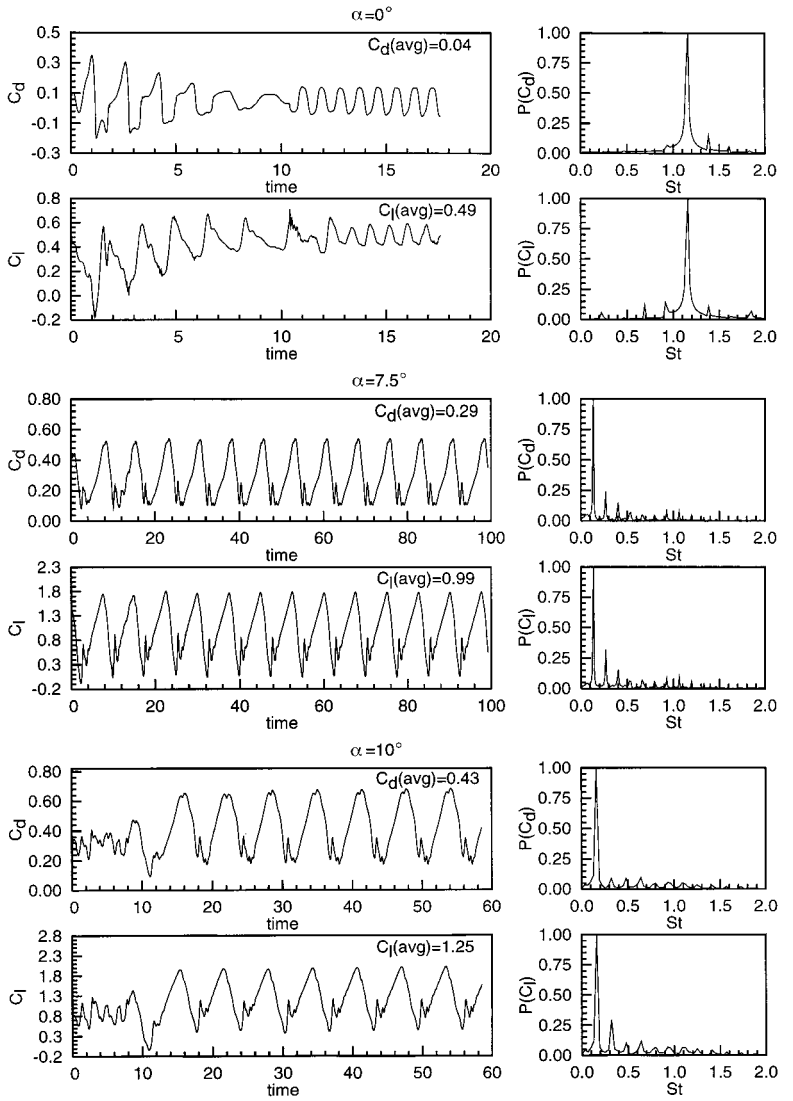

Figure 10. $Re = 10^6$ turbulent flow past a ram-air parafoil with $x_{\text{cut}} = 0.1c$ and $\theta_{\text{cut}} = 135°$ at various angles of attack: time histories of the lift and drag coefficients and their power spectra.

upper surface, the flow stays attached for a major part of the parafoil and a vortex is released at the trailing edge in each cycle of the lift coefficient variation while the flow separates right at the leading edge on the lower surface. Temporally periodic vortex shedding is observed. The time histories of the lift and drag coefficients and their time-averaged values are shown in

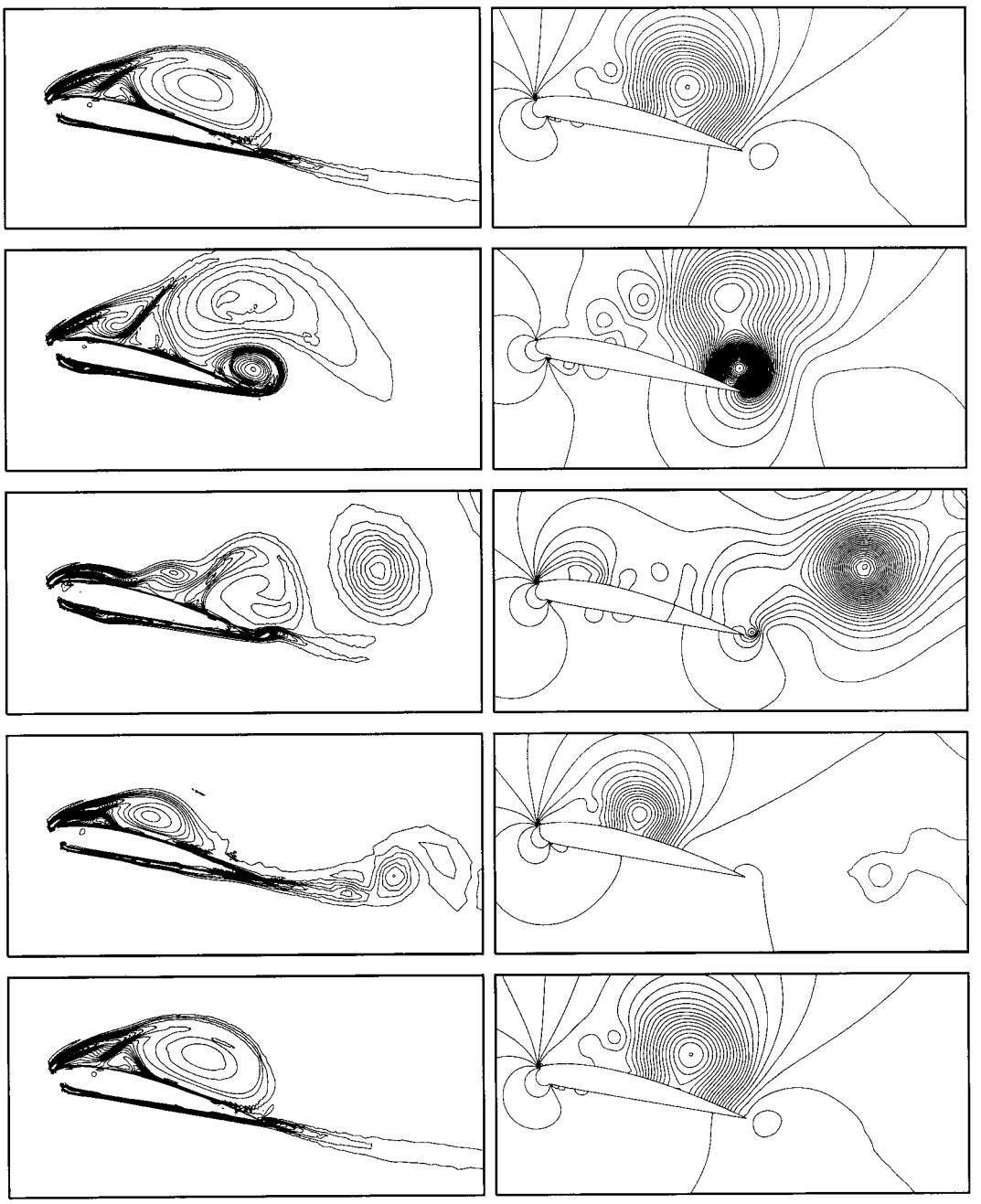

Figure 11. $Re = 10^6$ turbulent flow past a ram-air parafoil with $x_{cut} = 0.1c$ and $\theta_{cut} = 135°$ at $\alpha = 7.5°$: vorticity (left) and pressure (right) fields during one cycle of the lift coefficient variation for the temporally periodic solution.

Figure 10. After an initial transience, the flow settles to a time periodic state. It is interesting to note that the lift coefficient for a clean Clarck-Y airfoil at $\alpha = 0°$ is 0.68 (as predicted by the panel method), while the time-averaged value for the parafoil at the same angle is 0.49. The loss in the mean value of the lift and the appearance of unsteadiness is an artifact of the leading edge cut. Figure 11 shows the vorticity and pressure fields during one cycle of the lift coefficient for the temporally periodic solution for $\alpha = 7.5°$. Compared with the laminar flow for $\alpha = 7°$ (Plate 1) the flow in the present case is quite different. The vortices are larger and the wake is more organized. The time histories of the lift and drag coefficients and their power spectra are shown in Figure 10. The mean values of the lift and drag coefficients are 0.99 and 0.29 respectively. For the Clarck-Y airfoil without a leading edge cut the corresponding values are 1.38 and 0.0204. The leading edge cut leads to a loss of lift and a very large increase in drag. The lift-to-drag ratio reduces from 67.65 to 3.41. These values are in good agreement with those reported by other researchers [3,9]. It can be observed that in addition to the dominant vortex shedding frequency, certain other frequencies corresponding to the secondary and tertiary vortices are also present in the power spectra of the aerodynamic coefficients. The peak value of the lift coefficient corresponds to the instant when the large clockwise rotating vortex is fully developed and sits on the upper surface of the parafoil causing an increased suction. During each cycle of lift coefficient a clockwise rotating vortex is shed from the upper surface and a counter-clockwise rotating vortex is shed from the lower surface at the trailing edge. Figure 12 shows the variation of the pressure coefficient on the inner and outer surface

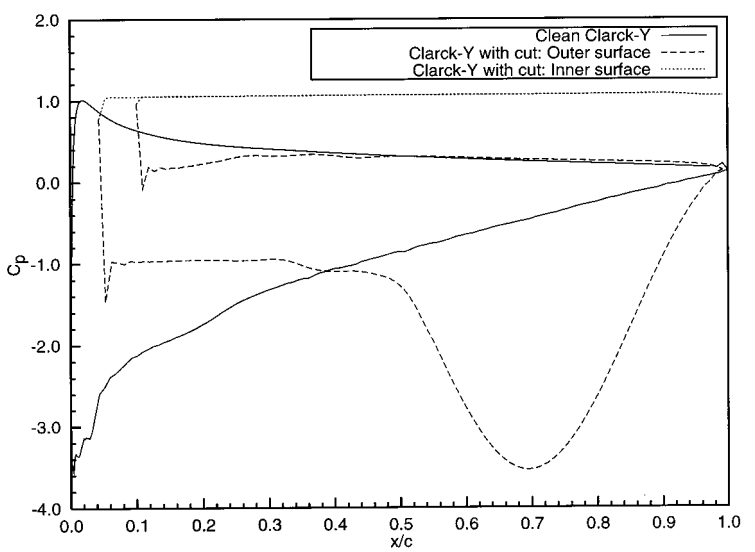

Figure 12. $Re = 10^6$ turbulent flow past a ram-air parafoil with $x_{cut} = 0.1c$ and $\theta_{cut} = 135°$ at $\alpha = 7.5°$: variation of the pressure coefficient on the inner and outer surface of the parafoil corresponding to the peak value of lift coefficient. Also shown is the pressure distribution for the Clarck-Y airfoil without a leading edge cut.

of the parafoil corresponding to the peak value of the lift coefficient. The pressure distribution on a Clarck-Y airfoil without a leading edge cut is also shown in the same figure for comparison. The pressure on the inner surface of the parafoil assumes an almost constant value that is equal to the stagnation pressure. The pressure variation on the outer surface of the parafoil and the Clarck-Y airfoil are quite different. The leading edge cut results in a significant loss in lift because of two major effects. As can be noticed from the C_p distribution on the Clarck-Y airfoil, the region near the leading edge contributes significantly to the total lift. The cut leads to an effective loss in the size of the body at the leading edge and therefore a loss in the lift. Also, the reduced values of the suction on the upper and high pressure on the lower surfaces cause a loss in the pressure differential across the airfoil, thereby reducing the net lift acting on the parafoil. The presence of a vortex on the upper surface on the parafoil does contribute to the lift. However, this is an unsteady effect and its contribution to the time-averaged value is not large enough to make up for the overall loss in lift. Figure 13 shows the flow field during one cycle of the lift coefficient for the temporally periodic solution for $\alpha = 10°$. The time histories for the aerodynamic coefficients for this case are shows in Figure 10. Qualitatively, the flow looks quite similar to that at $\alpha = 7.5°$. The lift-to-drag ratio for the time-averaged values of the aerodynamic coefficients is 2.91.

Shown in Figure 14 is the summary of the various aerodynamic coefficients related to the computations reported so far in this article. It is interesting to note that despite the differences in the time histories of the aerodynamic coefficients, the average values of the lift and drag coefficients at various angles of attack from laminar and turbulent flow computations for the parafoil are quite similar. This perhaps is due to the flow separation at the sharp corners of the leading edge cut for both the laminar and turbulent flows. The Strouhal number, related to the dominant frequency in the time variation of the lift coefficient, is lower for the turbulent flow computations. For both cases, the Strouhal number decreases with an increase in the angle of attack. This observation is consistent with that made by other researchers in the past [27]. As was observed earlier in the article, the laminar flow computations for the parafoil suggest a stall at an angle of attack of 10°. This is also evident from the drag–polar curve shown in the third row of Figure 14.

4.4. $Re = 10^6$ turbulent flow past a ram-air parafoil: effect of the size and location of the leading edge cut

It has been shown in the previous section that compared with the Clarck-Y airfoil, the parafoil section with a leading edge cut is associated with a significantly higher drag coefficient and a lower lift coefficient. This suggests that the location and the size of the cut may play an important role in the aerodynamic performance of the parafoil. To investigate this effect, computations are carried out for a parafoil at 7.5° angle of attack with two configurations of the leading edge cut: (a) $x_{cut} = 0.1c$, $\theta_{cut} = 150°$ and (b) $x_{cut} = 0.05c$, $\theta_{cut} = 135°$. The results for the leading edge cut with $x_{cut} = 0.1c$ and $\theta_{cut} = 135°$ have already been presented in the previous section. These three computations are expected to bring out the effect of x_{cut} and θ_{cut}. Plate 2 shows the vorticity and pressure fields for the three configurations of the leading edge cut corresponding to the peak value of the lift coefficient. The flow on the upper surface for all three cases looks very similar. However, there are differences in the flow on the lower

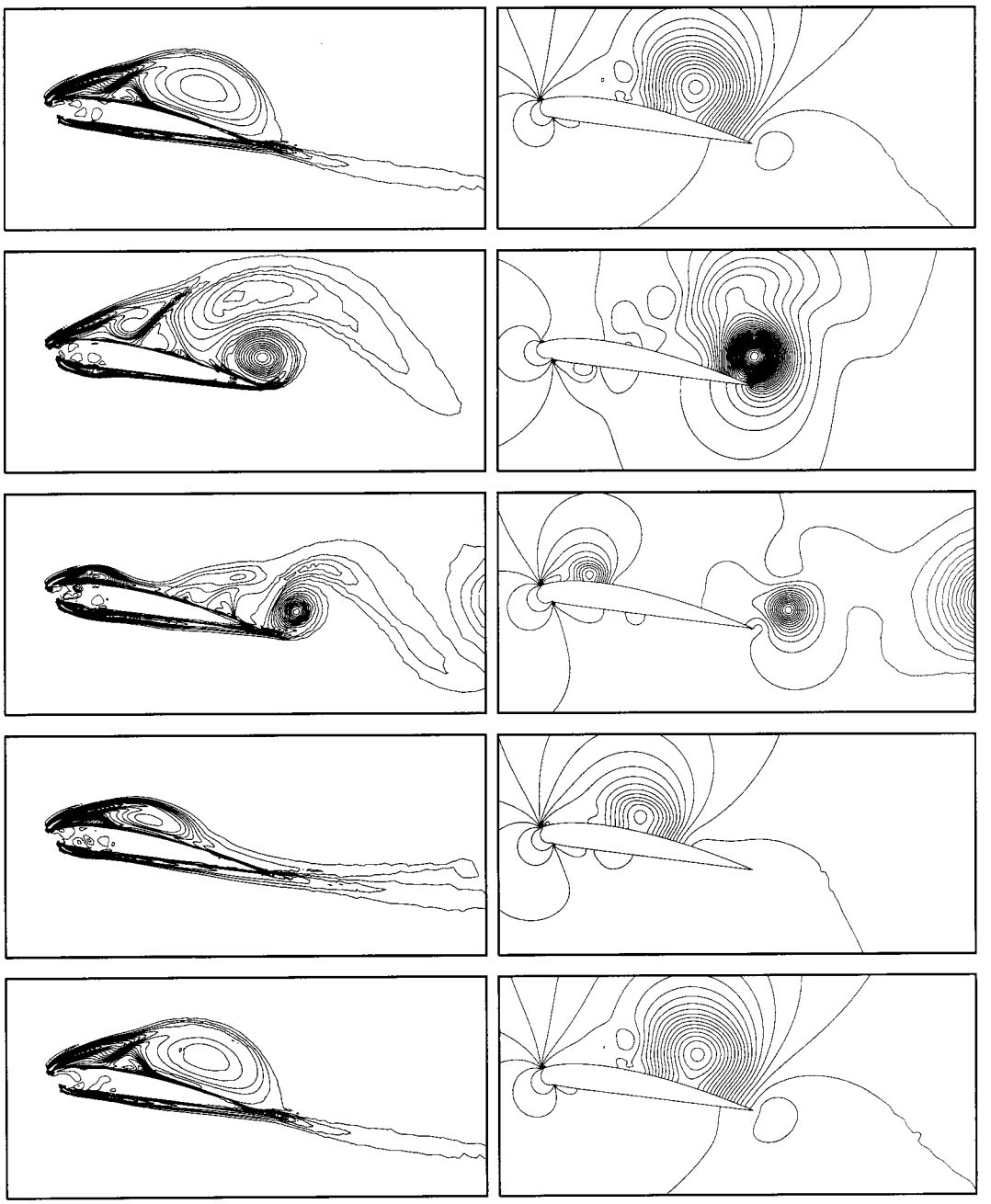

Figure 13. $Re = 10^6$ turbulent flow past a ram-air parafoil with $x_{cut} = 0.1c$ and $\theta_{cut} = 135°$ at $\alpha = 10°$: vorticity (left) and pressure (right) fields during one cycle of the lift coefficient variation for the temporally periodic solution.

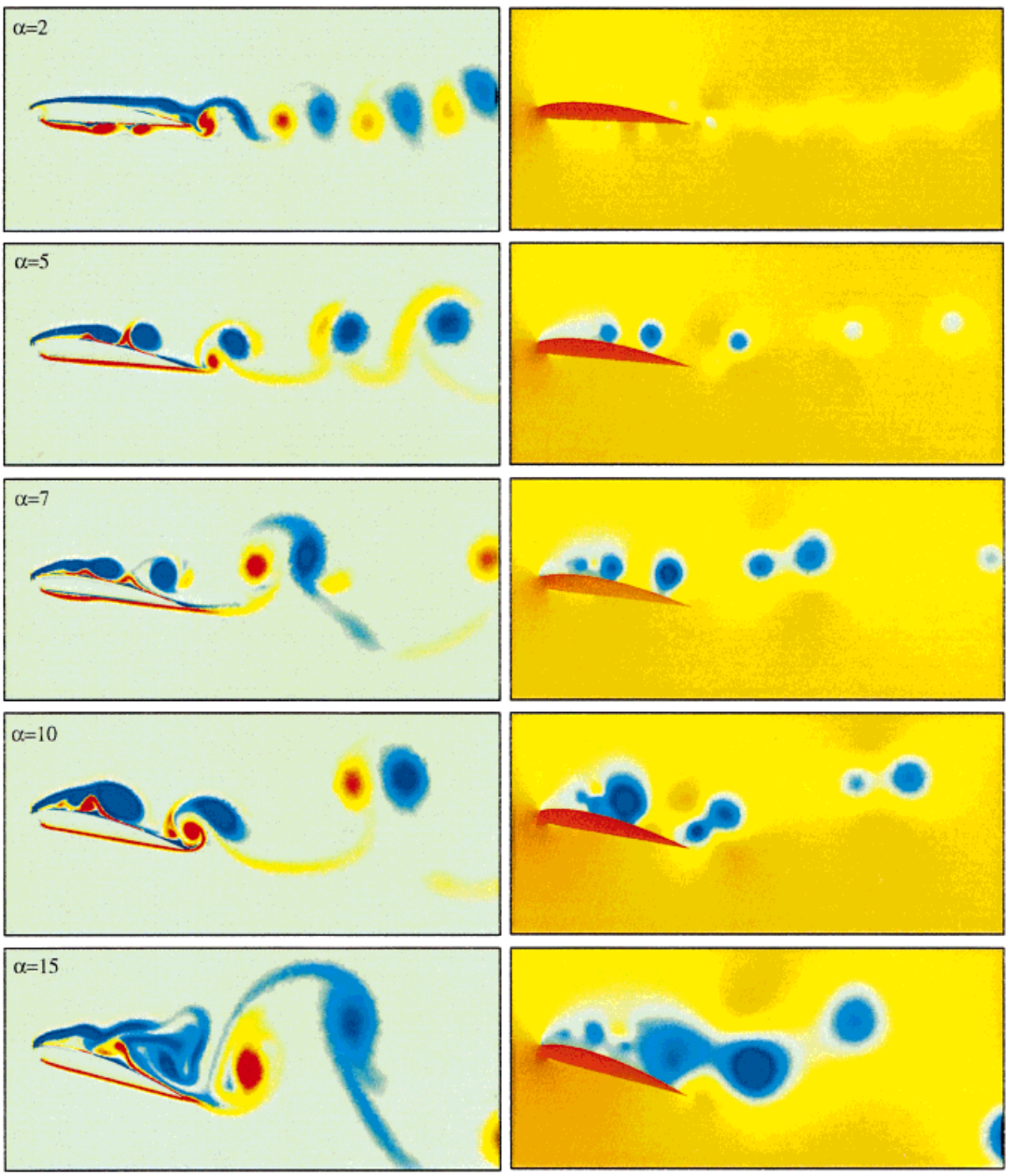

Plate 1. $Re = 10^4$ laminar flow past a ram-air parafoil with $x_{cut} = 0.1c$ and $\theta_{cut} = 135°$ at various angles of attack: vorticity (left) and pressure (right) fields corresponding to the peak value of the lift coefficient for the developed unsteady solution.

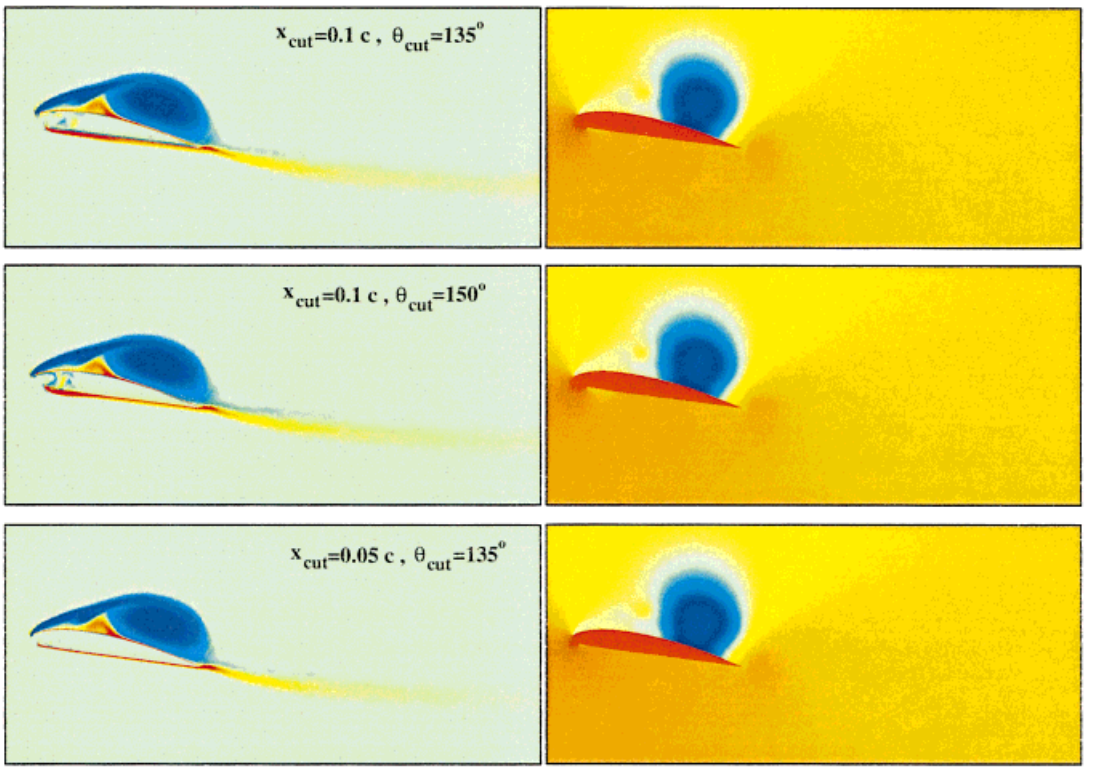

Plate 2. $Re = 10^6$ turbulent flow past a ram-air parafoil at $\alpha = 7.5°$: vorticity (left) and pressure (right) fields corresponding to the peak value of the lift coefficient for three configurations of the leading edge cut.

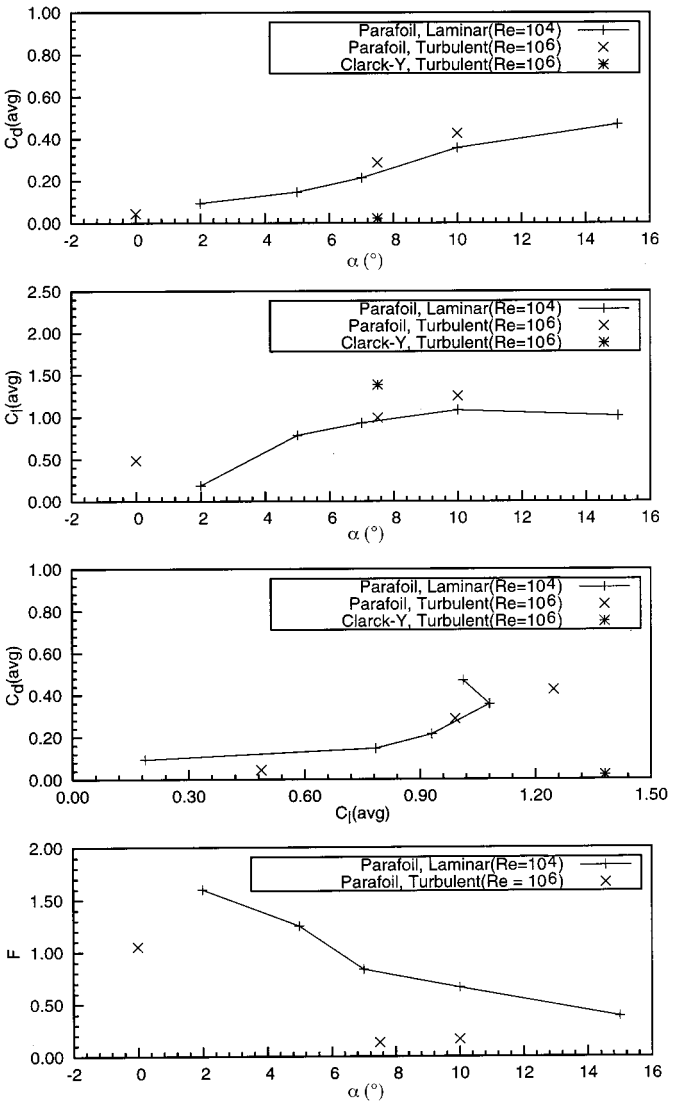

Figure 14. Flow past a ram-air parafoil with $x_{cut} = 0.1c$ and $\theta_{cut} = 135°$: variation of the aerodynamic coefficients with the angle of attack.

surface of the parafoil. The case with $x_{cut} = 0.05c$ is associated with a completely attached flow while there are separation bubbles close to the leading edge in the other two cases. This is also evident from the C_p plots on the outer surface of the parafoil for the three cases as shown in Figure 15. These figures suggest that the aerodynamic performance of the parafoil with

$x_{cut} = 0.05c$ and $\theta_{cut} = 135°$ is the best. This is confirmed by the time histories of the aerodynamic coefficients for the three cases as shown in Figure 16. A summary of the time-averaged values of the aerodynamic coefficients is presented in Table I. It can be observed from the table that Case 3 results in the best value of the lift-to-drag ratio and therefore this parafoil may be expected to have the best glide ratio amongst the three cases. A large leading edge cut modifies the flow past an airfoil significantly and deteriorates its aerodynamic performance. A very small cut close to the stagnation point of the airfoil is expected to lead to the best aerodynamic performance. However, the location of the stagnation point changes with the angle of attack and a very small cut may lead to an unacceptable duration of the inflation stage. Therefore, the configuration of the leading edge cut is usually a compromise between good aerodynamic performance in the glide stage and certain other issues related to the inflation stage of the parafoil.

5. CONCLUDING REMARKS

Results have been presented for computation of flow past a ram-air parachute with a leading edge cut. Both laminar ($Re = 10^4$) and turbulent ($Re = 10^6$) flows have been computed. The turbulent flows have been computed using the Baldwin–Lomax model. A well-proven stabilized FEM, which has been applied to various flow problems previously, has been used to solve the incompressible Navier–Stokes equations in the primitive variables formulation. Turbulent

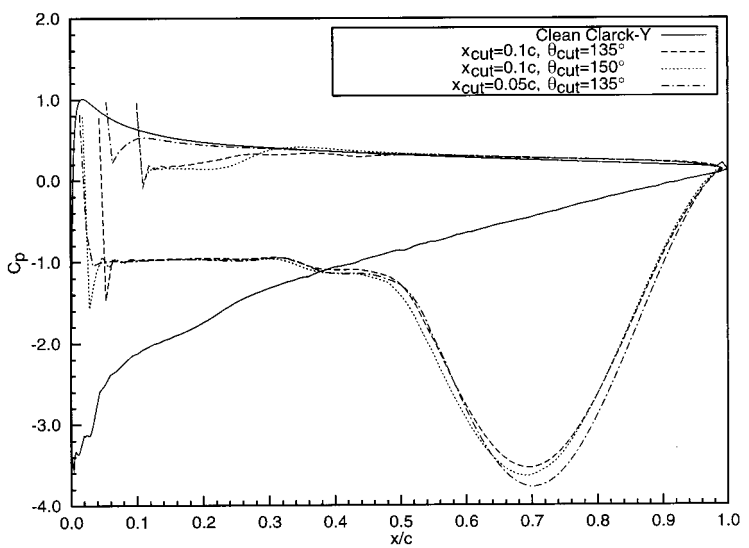

Figure 15. $Re = 10^6$ turbulent flow past a ram-air parafoil at $\alpha = 7.5°$: variation of the pressure coefficient along the outer surface of the parafoil corresponding to the peak value of the lift coefficient for three configurations of the leading edge cut.

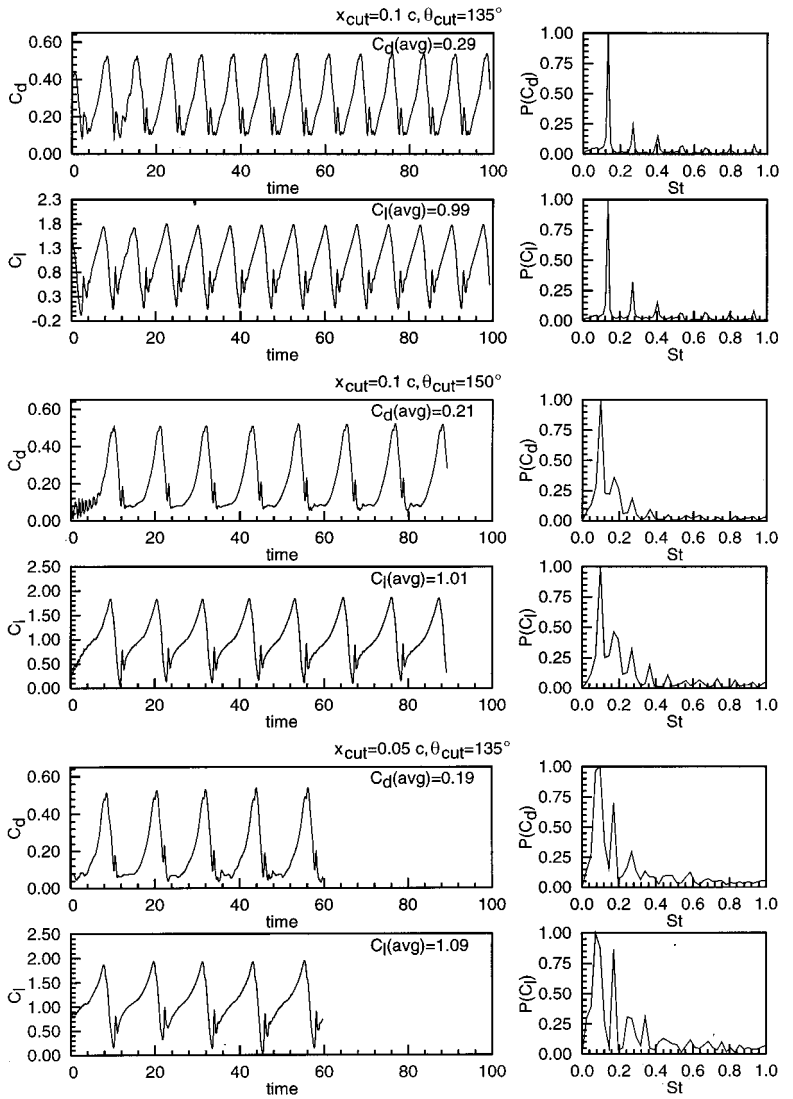

Figure 16. $Re = 10^6$ turbulent flow past a ram-air parafoil at $\alpha = 7.5°$: time histories of the lift and drag coefficients and their power spectra for three configurations of the leading edge cut.

flow computations past a Clarck-Y airfoil without a leading edge cut for $\alpha = 7.5°$ result in an attached flow. The sharp corners at the leading edge cut cause flow separation and result in unsteady flows even for small angles of attack. A significant loss in lift and an increase in drag compared with the Clarck-Y airfoil are observed. The flow inside the parafoil cell remains almost stagnant resulting in a high value of pressure that is responsible for giving the parafoil

Table I. $Re = 10^6$ turbulent flow past a ram-air parafoil for various configurations of the leading edge cut: time-averaged values of the lift and drag coefficients.

Case	x_{cut}	θ_{cut} (°)	C_l	C_d	C_l/C_d
1	$0.1c$	135	0.99	0.29	3.41
2	$0.1c$	150	1.01	0.21	4.81
3	$0.05c$	135	1.09	0.19	5.74

its shape. The values of the lift-to-drag ratio obtained with the present computations are in good agreement with those reported in the literature. The effect of the configuration of the leading edge cut on the flow is investigated. In all the cases considered the flow remains unsteady. The leading edge cut has a strong influence on the lift-to-drag ratio. While the flow on the upper surface of the parafoil is fairly insensitive, the flow quality on the lower surface improves as the leading edge cut becomes smaller and moves closer to the location of stagnation point for the basic airfoil section. It is observed that even though the time histories of the aerodynamic coefficients from the laminar and turbulent flow computations are quite different, their time-averaged values are quite similar. In future, this formulation may be coupled with a code that calculates the structural deformation of the parafoil and may be utilized to compute more realistic results that include the aeroelastic effects. In the present computations, the parafoil is assumed to have the shape of a truncated Clarck-Y airfoil. However, this is not the case in reality as suggested by wind tunnel tests conducted by other researchers. As a result of the unsteady flow, the shape of the parafoil gets modified and one may observe flutter of the parafoil fabric, especially, near the nose region.

ACKNOWLEDGMENTS

Partial support for this work has come from the Aeronautical Research and Development Board, India under the project number ARDB-AE-970310 with the Department of Aerospace Engineering, IIT Kanpur.

REFERENCES

1. Dennis DR. Recent advances in parachute technology. *Aeronautical Journal* 1983; **November**: 333–341.
2. Nicolaides JD, Speelman RJ III, Menard GLC. A review of parafoil applications. *Journal of Aircraft* 1970; **7**: 423–431.
3. Lingard JS. The aerodynamics of gliding parachutes. AIAA Paper 86-2427-CP, 1986.
4. Strickland JH, Higuchi H. Parachute aerodynamics: an assessment of prediction capability. *Journal of Aircraft* 1996; **33**: 709–749.
5. Benney RJ, Stein KR. Computational fluid-structure interaction model for parachute inflation. *Journal of Aircraft* 1996; **33**: 730–736.
6. Garrard WL, Tezduyar TE, Aliabadi SK, Kalro V, Luker J, Mittal S. Inflation analysis ram air inflated gliding parachutes. *Proceedings of AIAA 13th Aerodynamic Decelerator and Systems Conference*, Clearwater, FL, 1995; 186–189. AIAA Paper 95-1565.
7. Aliabadi SK, Garrard WL, Kalro V, Mittal S, Tezduyar TE, Stein KR. Parallel finite element computations of the dynamics of large ram air parachutes. *Proceedings of AIAA 13th Aerodynamic Decelerator and Systems Conference*, Clearwater, FL, 1995; 278–293. AIAA Paper 95-1581.

8. Tezduyar T, Kalro V, Garrard W. Parallel computational methods for 3D simulation of a parafoil with prescribed shape changes. Technical Report 96-082, AHPCRC, 1996.
9. Ross JC. Computational aerodynamics in the design and analysis of ram-air-inflated wings. *Proceedings of RAeS/AIAA 12th Aerodynamic Decelerator Systems Technology Conference and Seminar*, London, UK, 1993. AIAA Paper 93-1228.
10. Baldwin B, Lomax H. Thin layer approximation and algebraic turbulence model for separated turbulent flows. *Proceedings of AIAA 16th Aerospace Sciences Meeting*, Huntsville, AL, 1978. AIAA Paper 78-257.
11. Kallinderis Y. Algebraic turbulence modeling for adaptive unstructured grids. *AIAA Journal* 1992; **30**: 631–639.
12. Mavriplis DJ. Turbulent flow calculations using unstructured and adaptive meshes. *International Journal for Numerical Methods in Fluids* 1991; **13**: 1131–1152.
13. Anderson WK, Bonhaus DL. An implicit upwind algorithm for computing turbulent flows on unstructured grids. *Computers and Fluids* 1994; **23**: 1–21.
14. Hoffmann JA. Effects of freestream turbulence on the performance characteristics of an airfoil. *AIAA Journal* 1991; **29**(9): 1353–1354.
15. Tezduyar TE, Mittal S, Ray SE, Shih R. Incompressible flow computations with stabilized bilinear and linear equal-order-interpolation velocity-pressure elements. *Computer Methods in Applied Mechanics and Engineering* 1992; **95**: 221–242.
16. Hughes TJR, Brooks AN. A multi-dimensional upwind scheme with no crosswind diffusion. In *Finite Element Methods for Convection Dominated Flows*, vol. 34, Hughes TJR (ed.). ASME: New York, 1979; 19–34.
17. Hughes TJR, Tezduyar TE. Finite element methods for first-order hyperbolic systems with particular emphasis on the compressible Euler equations. *Computer Methods in Applied Mechanics and Engineering* 1984; **45**: 217–284.
18. Mittal S. On the performance of high aspect-ratio elements for incompressible flows. *Computer Methods in Applied Mechanics and Engineering* 2000; **188**: 269–287.
19. Saad Y, Schultz M. GMRES: a generalized minimal residual algorithm for solving nonsymmetric linear systems. *SIAM Journal of Scientific and Statistical Computing* 1986; **7**: 856–869.
20. Mittal S, Raghuvanshi A. Control of vortex shedding behind circular cylinder for flow at low Reynolds numbers. *International Journal for Numerical Methods in Fluids* 2001; **35**: 421–447.
21. Mittal S, Kumar V, Raghuvanshi A. Unsteady incompressible flow past two cylinders in tandem and staggered arrangements. *International Journal for Numerical Methods in Fluids* 1997; **25**: 1315–1344.
22. Behr M, Liou J, Shih R, Tezduyar TE. Vorticity–stream function formulation of unsteady incompressible flow past a cylinder: sensitivity of the computed flow field to the location of the outflow boundary. *International Journal for Numerical Methods in Fluids* 1991; **12**: 323–342.
23. Behr M, Hastreiter D, Mittal S, Tezduyar TE. Incompressible flow past a circular cylinder: dependence of the computed flow field on the location of the lateral boundaries. *Computer Methods in Applied Mechanics and Engineering* 1995; **123**: 309–316.
24. Katz J, Plotkin A. *Low-Speed Aerodynamics. From Wing Theory to Panel Methods*. McGraw-Hill: New York, 1991.
25. Mittal S, Tezduyar TE. Massively parallel finite element computation of incompressible flows involving fluid–body interactions. *Computer Methods in Applied Mechanics and Engineering* 1994; **112**: 253–282.
26. Behr M. Stabilized finite element methods for incompressible flows with emphasis on moving boundaries and interfaces. PhD thesis, Department of Aerospace Engineering, University of Minnesota, 1992.
27. Blevins RD. *Flow-induced Vibration*. Van Nostrand Reinhold: New York, 1990.

